Decoupling indirect topographic cross-talk in band excitation piezoresponse force microscopy imaging and spectroscopy

Sang Mo Yang, Lucie Mazet, M. Baris Okatan, Stephen Jesse, Gang Niu, Thomas Schroeder, Sylvie Schamm-Chardon, Catherine Dubourdieu, Arthur P. Baddorf, Sergei V. Kalinin

Decoupling indirect topographic cross-talk in band excitation piezoresponse force microscopy imaging and spectroscopy

Sang Mo Yang, Lucie Mazet, M. Baris Okatan, Stephen Jesse, Gang Niu, Thomas Schroeder, Sylvie Schamm-Chardon, Catherine Dubourdieu, Arthur P. Baddorf, and Sergei V. Kalinin

Citation: Appl. Phys. Lett. **108**, 252902 (2016); doi: 10.1063/1.4954276
View online: https://doi.org/10.1063/1.4954276
View Table of Contents: http://aip.scitation.org/toc/apl/108/25
Published by the American Institute of Physics

Decoupling indirect topographic cross-talk in band excitation piezoresponse force microscopy imaging and spectroscopy

Sang Mo Yang,[1,a)] Lucie Mazet,[2] M. Baris Okatan,[1] Stephen Jesse,[1] Gang Niu,[3,b)] Thomas Schroeder,[3] Sylvie Schamm-Chardon,[4] Catherine Dubourdieu,[2,c)] Arthur P. Baddorf,[1] and Sergei V. Kalinin[1,a)]
[1]*Center for Nanophase Materials Sciences, Oak Ridge National Laboratory, Oak Ridge, Tennessee 37831, USA*
[2]*Institut des Nanotechnologies de Lyon, CNRS UMR 5270, Ecole Centrale de Lyon, Université de Lyon, 69134 Ecully, France*
[3]*IHP—Innovations for High Performance Microelectronics, Im Technologiepark 25, 15236 Frankfurt (Oder), Germany*
[4]*CEMES-CNRS, Université de Toulouse, 29 rue Jeanne Marvig, F-31055 Toulouse, France*

(Received 8 February 2016; accepted 2 June 2016; published online 20 June 2016)

All scanning probe microscopies are subjected to topographic cross-talk, meaning the topography-related contrast in functional images. Here, we investigate the signatures of indirect topographic cross-talk in piezoresponse force microscopy (PFM) imaging and spectroscopy and its decoupling using band excitation (BE) method in ferroelectric $BaTiO_3$ deposited on the Si substrates with free standing nanopillars of diameter 50 nm. Comparison between the single-frequency PFM and BE-PFM results shows that the measured signal can be significantly distorted by topography-induced shifts in the contact resonance frequency and cantilever transfer function. However, with proper correction, such shifts do not affect PFM imaging and hysteresis loop measurements. This suggests the necessity of an advanced approach, such as BE-PFM, for detection of intrinsic sample piezoresponse on the topographically non-uniform surfaces. *Published by AIP Publishing.*
[http://dx.doi.org/10.1063/1.4954276]

In the past two decades, piezoresponse force microscopy (PFM) has emerged as an indispensable tool for characterizing local electromechanical response in various materials, such as inorganic ferroelectrics and multiferroics,[1–3] ferroelectric polymers,[4–7] and biological systems.[8,9] PFM measures an electrical bias-induced sample deformation. Application of an AC bias with a frequency ω to a conductive tip generates a periodic surface displacement due to the converse piezoelectric effect. In this conventional single-frequency PFM, the response is measured by a lock-in amplifier, yielding amplitude, and phase signals, which contain information about the local piezoresponse magnitude and polarization orientation, respectively.

Since the early days of PFM, it has become obvious that surface topography can strongly couple to the measured PFM signal.[10,11] In particular, PFM is very sensitive to *indirect* topographic cross-talk rather than the direct morphology effect (such as contact radius dependence of the PFM signal).[11,12] The mechanism of indirect topographic cross-talk can be understood as follows. The measured PFM signal is a product of intrinsic sample piezoresponse and cantilever transfer function.[12] The latter is primarily determined by the mechanical property of the tip-surface junction, such as contact stiffness. Most real materials are topographically non-uniform so that the contact stiffness varies with sample position, even on piezoelectrically uniform surfaces. Consequently, surface topography shifts the local cantilever transfer function, leading to the changes in the measured PFM signal.[11] This indirect topographic cross-talk effect is particularly pronounced where ω is close to a contact resonance frequency of the cantilever ω_r (typically, hundreds kHz), since the response varies drastically with a small shift in the transfer function. To avoid severe topographic cross-talk, single-frequency PFM measurements are typically performed at a low frequency (well below ω_r), where the transfer function is less dependent on ω. However, even the low frequency response can be still affected by a non-ideal transfer function.[13] Furthermore, low frequency PFM does not take a big advantage of signal amplification at the ω_r, precluding the studies of weakly piezoelectric materials, such as ultrathin ferroelectric films and biological systems.

To minimize topographic cross-talk and enhance signal-to-noise (S/N) ratio simultaneously, advanced PFM approaches using multiple frequencies have been developed, such as dual AC resonance tracking (DART)[14] or band excitation (BE).[12,15] These methods allow continuous detection of the electromechanical response at the local ω_r. In particular, the BE method captures all responses within a band of frequencies around ω_r, enabling deconvolution of all parameters of the cantilever transfer function, including ω_r, quality factor, response amplitude, and phase.[12] In this manner, the BE technique can separate intrinsic PFM response (response amplitude and phase) from topographic and elastic properties of the tip-surface junction (ω_r and quality factor). However, despite the very broad range of studies by BE-PFM,[12,16] the decoupling quality of indirect topographic cross-talk in BE-PFM has not yet been

[a)]Authors to whom correspondence should be addressed. Electronic addresses: yangs@ornl.gov and sergei2@ornl.gov
[b)]Present address: Electronic Materials Research Laboratory, Key Laboratory of the Ministry of Education & International Center for Dielectric Research, Xi'an Jiaotong University, Xi'an 710049, China.
[c)]Present address: Helmholtz Zentrum Berlin für Materialien und Energie, IFOX, Hahn-Meitner-Platz 1, 14109 Berlin, Germany.

fully ascertained. To confirm it, one has to show that the surface morphology shifts the cantilever transfer function and thus the PFM signal is distorted. (i.e., the signatures of indirect topographic cross-talk). However, ω_r is strongly dependent on the material property as well as topographic property so that it is difficult to distinguish if the variation of ω_r originates from solely topographic cross-talk effect. Therefore, to establish the decoupling quality of the topographic cross-talk in BE-PFM, the sample should be required to be materially uniform with only different topography.

Here, we explore the signatures of indirect topographic cross-talk and its decoupling in BE-PFM imaging and spectroscopy. As a model system, we chose the $BaTiO_3$ (BTO) film grown by molecular beam epitaxy (MBE) on $SrTiO_3$ (STO)-buffered Si(100) substrates featuring free standing 100-nm-high nanopillars of diameter 50 nm (Fig. 1(a)). The silicon nanopillars were fabricated by ultraviolet lithography (KrF deep-UV Nikon Scanner S207) and subsequent plasma etching, as described in detail in Ref. 17. Their pitch distance (from center to center) is about 250 nm (Figs. 1(a) and 1(b)). A 3-nm-thick STO buffer was deposited by MBE on the prepared Si structure at 400 °C under an oxygen partial pressure $P(O_2)$ of 5×10^{-8} Torr. Subsequently, BTO (~14 nm thickness) was grown at 525 °C under $P(O_2) = 5 \times 10^{-7}$ Torr. Then, the sample was cooled at 25 °C min^{-1} under vacuum (5×10^{-8} Torr) to room temperature. A thin SiO_2 layer formed at the STO/Si interface during the BTO growth and post-deposition annealing.[18] A detailed description of the BTO and STO epitaxial growth has been published elsewhere.[18] X-ray diffraction result showed that $BaTiO_3$ crystallizes in a tetragonal structure with *c*-axis orientation, perpendicular to the substrate's plane (not shown here). In similar growth conditions on fully planar silicon, the $BaTiO_3$ films were found to be ferroelectric.[18,19] As shown in Fig. 1(a), the BTO/STO stacks were grown on top of the silicon pillars as well as in the region between the pillars (referred to as the "etched region" hereinafter). However, as MBE is not a technique allowing conformal coverage, the BTO/STO stacks were not well grown on the sidewalls of the pillars (those regions appear amorphous). In this paper, we will focus on the PFM response in the etched regions and on top of the pillars.

BE-PFM measurements were performed using a commercial atomic force microscope (Cypher, Asylum Research) interfaced with National Instrument cards controlled by Labview/Matlab software. Pt/Cr-coated conductive tips (Budget Sensors, Multi75E-G) were used for the measurements. Imaging and data processing were performed using WSxM[20] and custom-written Matlab codes, respectively.

We first performed single-frequency PFM imaging on the BTO/STO/(SiO_2)/Si heterostructures. Since the sample has no bottom electrode and the thickness of BTO layer is relatively thin, for high S/N ratio we used a 1 V AC bias with 324 kHz (close to the first ω_r). As shown in Fig. 1(c), a topographic image ($900 \times 900\ nm^2$) of the sample shows nanopillar regions and the etched region in between. To explore additional topography effects by the pillar, we chose the probing region with one pillar broken before imaging (the solid green arrow). The observed asymmetric and broad features of the pillar structures are due to the tip motion during contact mode imaging and the finite tip size.

The corresponding single-frequency PFM amplitude and phase images are shown in Figs. 1(d) and 1(e), respectively. In both images, the circular pillar regions can be easily differentiated from the surrounding etched region. By overlaying the phase image on the topographic image, the regions with distinct phase contrast (e.g., the open circle in Fig. 1(e)) are confirmed to be the top of the pillars. However, the amplitude signal is high in the whole upper half of the pillar regions, including a part of the pillar sidewalls (where the BTO films would not be crystallized) as well as the pillar tops. Particularly, the amplitude signal is high even in the region where the nanopillar is broken (presumably, Si or SiO_2 is exposed). Therefore, the amplitude signal has significant levels of distortion, illustrating a limitation of the single-frequency PFM.

We proceeded to carry out BE-PFM imaging at the same sample position. In BE-PFM imaging, a bias waveform consisting of multiple frequencies around ω_r (covering possible variations in ω_r during imaging) is applied. The simultaneously detected signals over time are Fourier-transformed to yield the raw data spectra over the frequency domain, which can be analyzed using a simple harmonic oscillator model, for which

$$A(\omega) = \frac{A_0 {\omega_r}^2}{\sqrt{\left(\omega^2 - {\omega_r}^2\right)^2 + \left(\omega\omega_r/Q\right)^2}}, \tag{1a}$$

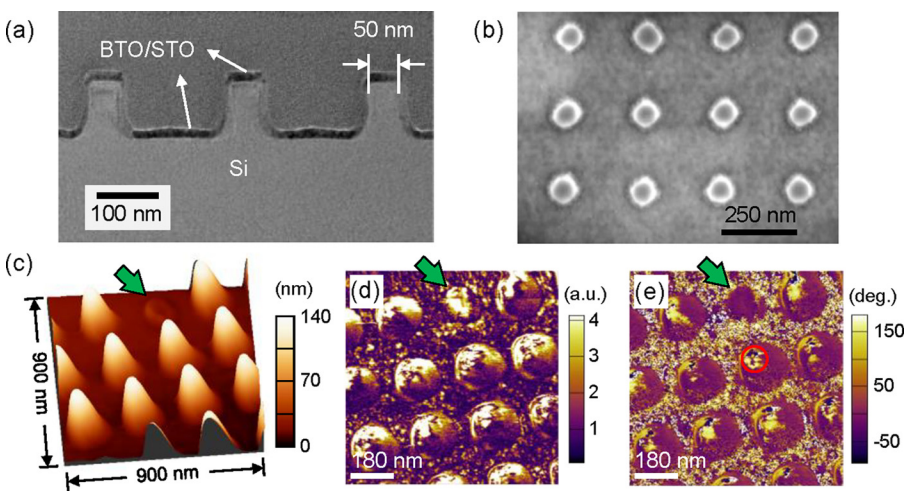

FIG. 1. (a) Cross-sectional transmission electron microscopy image and (b) top-view scanning electron microscopy image of the BTO/STO/(SiO_2)/Si heterostructures. The dark regions indicate the BTO/STO stacks grown by MBE. (c) A three-dimensional topographic image and the corresponding single-frequency PFM (d) amplitude and (e) phase images of the heterostructures. The solid green arrows in (c)–(e) indicate the region where a nanopillar was broken before imaging.

$$\varphi(\omega) = \arctan\left(\frac{\omega\omega_r/Q}{\omega^2 - {\omega_r}^2} + \varphi_0\right), \quad (1b)$$

where A is the frequency-dependent response amplitude, A_0 is the amplitude at ω_r, Q is the quality factor, φ is the frequency-dependent response phase, and φ_0 is the phase (offset) determined by local polarization orientation. The functional fit based on Eq. (1a) and (1b) yields A_0, φ_0, ω_r, and Q at each point, constructing a spatial map of each parameter, as shown in Figs. 2(a)–2(d). White pixels observed in the images (including Figs. 2–4) represent the points where the BE-PFM response was small, and thus, was not amendable to fitting.

The resonance frequency ω_r shown in Fig. 2(a) varies significantly with the topography; it changes in the pillar regions by up to 40 kHz, whereas it is relatively homogeneous in the etched regions. This indicates that the transfer function shifts strongly on topographically non-uniform pillar regions, as also seen in Fig. 2(e). The vertical dashed line in Fig. 2(e) indicates the operating frequency ω of 324 kHz used in the previous single-frequency PFM imaging. It is close to ω_r at position 1 (a side of the pillar) and position 2 (top of the pillar), whereas it is far away from resonances at position 3 (etched region) and position 4 (another side of the pillar). These differences between ω and local ω_r can explain

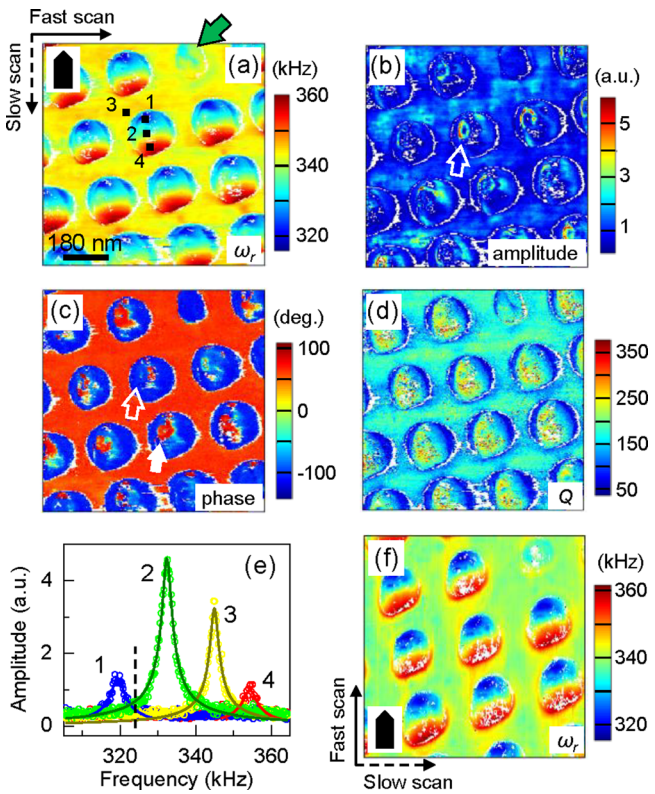

FIG. 2. Spatial maps of the BE-PFM (a) resonance frequency, (b) amplitude, (c) phase, and (d) quality factor. The solid arrow in (a) exhibits the nanopillar-broken region, indicating that the probing region is identical to Fig. 1. (e) BE-PFM amplitude vs. frequency at the four different regions marked in (a). The open circles and solid lines show the raw data and fitted data, respectively. (f) Spatial map of the resonance frequency measured at the same sample position under a different scan angle of −90° with respect to that used in (a). Consequently, the fast and slow scan directions are changed. The insets in (a) and (f) show the cantilever orientation.

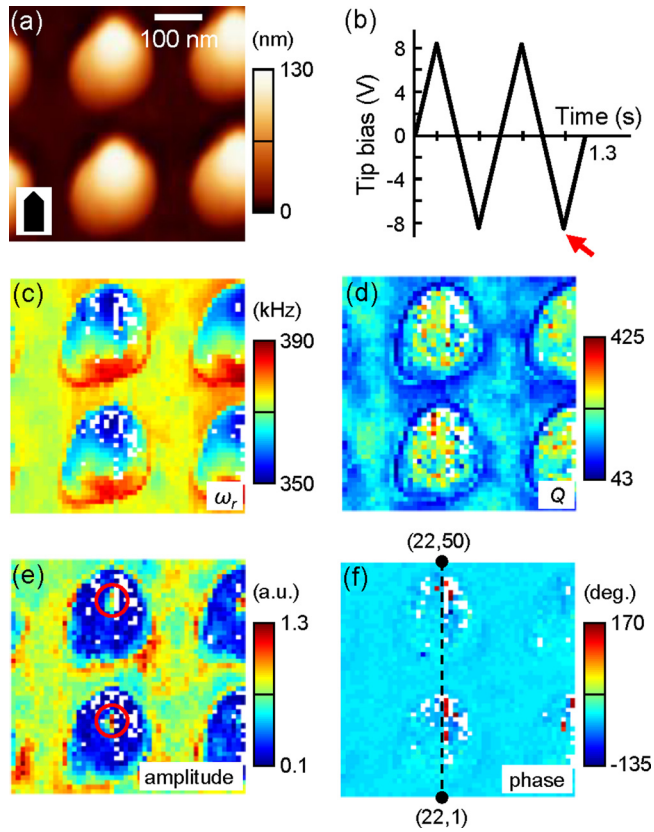

FIG. 3. (a) A topographic image ($500 \times 500\,nm^2$) of the BTO/STO/(SiO_2)/Si heterostructures. The scan angle was −90°, identical to that used in Fig. 2(f). (b) The triangular DC pulse used for BE-SSPFM measurement. The 50×50 grid ($500 \times 500\,nm^2$) spatial maps of the (c) resonance frequency, (d) quality factor, (e) amplitude, and (f) phase analyzed from the data recorded at $V_{dc} = -8.5$ V and the second cycle, as indicated by the arrow in (b). The open circles in (e) show the top regions of the pillars. The dashed line between the coordinates $(x,y) = (22,1)$ and (22,50) in (f) crosses the tops of two pillars. Note that (1,1) locates at the left bottom corner.

the artifacts observed in Fig. 1(d) as: (i) the signal in position 1 looked similar to that in position 2 and (ii) higher than that in position 3. Therefore, the signals in the previous single-frequency PFM were significantly distorted by indirect topographic cross-talk, i.e., topography-induced shifts in the transfer function.

However, the indirect topographic cross-talk can be decoupled in BE-PFM, since the sample response is measured at the ω_r at each point so that the ω_r variation does not affect the response amplitude A_0. For example, A_0 is obtained from the peak value at ω_r divided by local quality factor Q related to the mechanical property (see Eq. (1a)). The spatial map of BE-PFM amplitude in Fig. 2(b) differs considerably from the single-frequency amplitude image (Fig. 1(d)). One notable difference is a high response on top of the pillars, especially their outskirts (the open arrow in Fig. 2(b)). Such ring-shaped patterns may be related to different mechanical boundary conditions (such as strain relaxation at the pillar perimeters) or the other effects of topography, microfabrication, and/or non-uniform electric field in the material. In addition, the amplitude signal is almost zero in the nanopillar-broken region unlike the single-frequency PFM image in Fig. 1(d). These results illustrate the quality of decoupling of the topographic cross-talk effect in BE-PFM imaging.

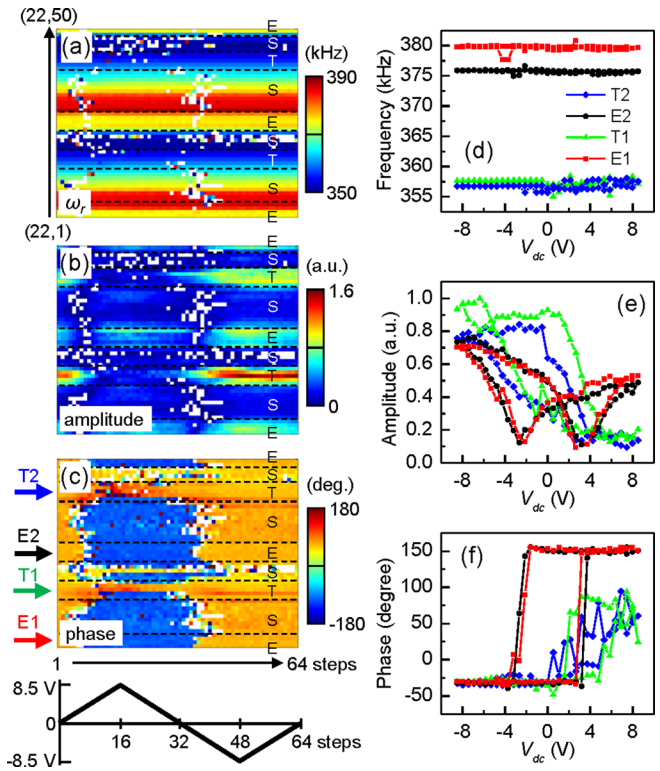

FIG. 4. The maps of (a) resonance frequency, (b) amplitude, and (c) phase vs. voltage step along the selected line in Fig. 3(f). The dashed lines separate the regions of the etched region ("E"), the sidewall of the pillar ("S"), and the top of the nanopillar ("T"). The relatively broad feature of "S" regions is due to the tip effect (see Fig. 3(a)). The hysteresis loops of the (d) resonance frequency, (e) amplitude, and (f) phase averaged over the tops of the pillars ("T1" and "T2") and the etched regions ("E1" and "E2"), as indicated by the arrows in (c).

The phase map in Fig. 2(c) also differs significantly from the single-frequency PFM phase image (Fig. 1(e)). The PFM phase signal is determined by the orientation of preponderant domains in the probing volume beneath the tip. In that sense, the as-grown BTO is nearly a monodomain state in the etched region (only the red contrast). The BTO on top of the pillars shows the ring-shaped patterns and their outskirt parts have either the red (the solid arrow) or the blue contrast (the open arrow), i.e., two dominant domain orientations. The Q value shown in Fig. 2(d) is almost homogeneous in the etched region, indicative of a uniform elastic property of the tip-surface junction. However, it becomes low at the circular boundaries between the pillars and the etched region. In the pillar regions, the Q value becomes increased again and inhomogeneous due to non-uniform surface morphology.

We found that the topography-induced variations in ω_r are also strongly affected by the cantilever orientation. As shown in Fig. 2(a), the ω_r value increases gradually from top to bottom of the image in the pillar regions; it is asymmetric along the long cantilever axis. Since the pillar structures are isotropic and symmetric, we first suspected the tip motion could make such ω_r variations. However, as seen in Fig. 2(f), the fast scan direction does not affect the shifts in ω_r. Instead, we found that the changes in ω_r always occur along the long cantilever axis (i.e., longitudinal direction). Even when the sample was rotated physically and imaged, the ω_r varied along the longitudinal direction (not shown here). Therefore, it can be concluded that the change in the cantilever dynamics along the longitudinal direction or an asymmetric tip apex plays an important role in the variations of ω_r rather than the inhomogeneity of the sample.

Next, to check the decoupling quality of BE method in spectroscopic measurements, we performed BE switching spectroscopy PFM (BE-SSPFM)[16] on the sample. In BE-SSPFM, an additional serve of DC pulse (V_{dc}) is applied to switch the local polarization. Here, we chose a region of $500 \times 500\,\text{nm}^2$ (Fig. 3(a)) and performed the measurements at a 50×50 grid of points using the triangular DC pulse illustrated in Fig. 3(b).

Examples of spatial maps of ω_r, Q, A_0, and φ_0 are shown in Figs. 3(c)–3(f), respectively. They were constructed from the data recorded at $V_{dc} = -8.5$ V and the second cycle. The maps of ω_r and Q are similar to Figs. 2(a) and 2(d) for as-grown states, indicative of no significant changes in mechanical properties under an application of V_{dc}. However, the maps of A_0 and φ_0 differ from Figs. 2(b) and 2(c), suggesting that the local polarization switching. The amplitude signal in the etched region shows as high as that in the pillar tops (Fig. 3(e)). This indicates that BTO is fully poled by -8.5 V in both regions, as also confirmed by the single phase contrast in Fig. 3(f).

Figures 4(a)–4(c) exhibit the maps of ω_r, A_0, and φ_0 along the dashed line in Fig. 3(f) as a function of the voltage step at the second cycle, respectively. The x- and y-axes of these maps are voltage steps (from 0 to 64, see the bottom panel of Fig. 4(c)) and spatial position (from (22,1) to (22,50) in Fig. 3), respectively. The mechanical property is almost the same with V_{dc} (Fig. 4(a)), whereas the piezoelectric property changes with the bias, indicative of ferroelectric polarization switching in BTO (Figs. 4(b) and 4(c)).

Here, we focus on the quality of decoupling between piezoelectric and mechanical properties in BE-SSPFM. Figure 4(d) shows the ω_r values as a function of V_{dc} averaged over the four different regions, as indicated by the arrows in Fig. 4(c). They differ depending on the position by up to 35 kHz. Even for the flat etched regions (i.e., E1 and E2), the difference between their average ω_r values is about 5 kHz. Nevertheless, the E1 and E2 regions show similar polarization switching behaviors with clear butterfly shaped amplitude signals (Fig. 4(e)) and almost 180° phase flips (Fig. 4(f)). That is, the intrinsic piezoresponse is almost identical in those regions even though their mechanical properties are different. This illustrates that the BE technique can improve the data quality even for topographically flat surfaces. In addition, BE-SSPFM allows us to probe the intrinsic piezoresponse on top of the pillars (i.e., T1 and T2) which is distinct from that on the etched regions (Figs. 4(e) and 4(f)). Considering the fact that the full-width-half-maximum of the transfer function is ~5 kHz (Fig. 2(e)), it is impossible to obtain these results using a single frequency. If a 380 kHz is chosen as the operating frequency (corresponding to the average ω_r value at the E1 region), the other three locations will show almost zero amplitude response. The observed different ferroelectric behaviors on top of the pillars will be further investigated.

In summary, we demonstrated how topography-induced cantilever transfer function shift affects the measured PFM signal and how such indirect topographic cross-talk effects are separated in BE-PFM. For this study, we investigated the BTO/STO heterostructures simultaneously grown on different

morphologies: on top of 100-nm-high Si nanopillars and on the etched Si region in between the pillars. We clearly showed that topography yields the variations in contact resonance frequency and consequently the cantilever transfer function as well. However, once the corrections are made, such indirect topographic cross-talk effects do not change the intrinsic sample response and hysteresis measurements. This work highlights that the decoupling between piezoelectric and topographic contrasts is necessary in PFM measurements on even topographically flat surfaces and in that sense the BE technique is powerful.

Data acquisition, analysis, and methods (S.M.Y., M.B.O., S.J., A.P.B., and S.V.K.) were supported by and conducted at the Center for Nanophase Materials Sciences, which is a DOE Office of Science User Facility. Materials synthesis work (L.M. and C.D.) was supported by the LABEX iMUST (ANR-10-LABX-0064) of Université de Lyon, within the program "Investissements d'Avenir" (ANR-11-IDEX-0007) operated by the French National Research Agency (ANR) and, together with the TEM work as well (S.S.-C.), by the Grant No. ANR-14-CE26-0010 (project INTENSE). Robin Cours from CEMES is acknowledged for his strong support on the TEM sample preparation.

[1]A. Gruverman and A. Kholkin, Rep. Prog. Phys. **69**, 2443 (2006).
[2]S. V. Kalinin, A. N. Morozovska, L. Q. Chen, and B. J. Rodriguez, Rep. Prog. Phys. **73**, 056502 (2010).
[3]S. M. Yang, J.-G. Yoon, and T. W. Noh, Curr. Appl. Phys. **11**, 1111 (2011).
[4]B. J. Rodriguez, S. Jesse, S. V. Kalinin, J. Kim, S. Ducharme, and V. M. Fridkin, Appl. Phys. Lett. **90**, 122904 (2007).
[5]R. Gysel, I. Stolichnov, A. K. Tagantsev, N. Setter, and P. Mokrý, J. Appl. Phys. **103**, 084120 (2008).
[6]P. Sharma, T. J. Reece, S. Ducharme, and A. Gruverman, Nano Lett. **11**, 1970 (2011).
[7]Y.-Y. Choi, J. Hong, S. Hong, H. Song, D.-S. Cheong, and K. No, Phys. Status Solidi RRL **4**, 94 (2010).
[8]S. V. Kalinin, B. J. Rodriguez, S. Jesse, T. Thundat, and A. Gruverman, Appl. Phys. Lett. **87**, 053901 (2005).
[9]Y. Liu, Y. Zhang, M.-J. Chow, Q. N. Chen, and J. Li, Phys. Rev. Lett. **108**, 078103 (2012).
[10]F. Peter, A. Rüdiger, R. Dittmann, R. Waser, K. Szot, B. Reichenberg, and K. Prume, Appl. Phys. Lett. **87**, 082901 (2005).
[11]S. Jesse, S. Guo, A. Kumar, B. J. Rodriguez, R. Proksch, and S. V. Kalinin, Nanotechnology **21**, 405703 (2010).
[12]S. Jesse and S. V. Kalinin, J. Phys. D: Appl. Phys. **44**, 464006 (2011).
[13]E. Soergel, J. Phys. D: Appl. Phys. **44**, 464003 (2011).
[14]B. J. Rodriguez, C. Callahan, S. V. Kalinin, and R. Proksch, Nanotechnology **18**, 475504 (2007).
[15]S. Jesse, S. V. Kalinin, R. Proksch, A. P. Baddorf, and B. J. Rodriguez, Nanotechnology **18**, 435503 (2007).
[16]S. Jesse, R. K. Vasudevan, L. Collins, E. Strelcov, M. B. Okatan, A. Belianinov, A. P. Baddorf, R. Proksch, and S. V. Kalinin, Annu. Rev. Phys. Chem. **65**, 519 (2014).
[17]J. Bauer, Y. Yamamoto, P. Zaumseil, O. Fursenko, K. Schulz, G. Kozlowski, M. A. Schubert, T. Schroeder, and B. Tillack, Microelectron. Eng. **97**, 169 (2012).
[18]L. Mazet, R. Bachelet, L. Louahadj, D. Albertini, B. Gautier, R. Cours, S. Schamm-Chardon, G. Saint-Girons, and C. Dubourdieu, J. Appl. Phys. **116**, 214102 (2014).
[19]L. Mazet, S. M. Yang, S. V. Kalinin, S. Schamm-Chardon, and C. Dubourdieu, Sci. Technol. Adv. Mater. **16**, 036005 (2015).
[20]I. Horcas, R. Fernández, J. M. Gómez-Rodríguez, J. Colchero, J. Gómez-Herrero, and A. M. Baro, Rev. Sci. Instrum. **78**, 013705 (2007).